Journal of Materials Chemistry A

Accepted Manuscript

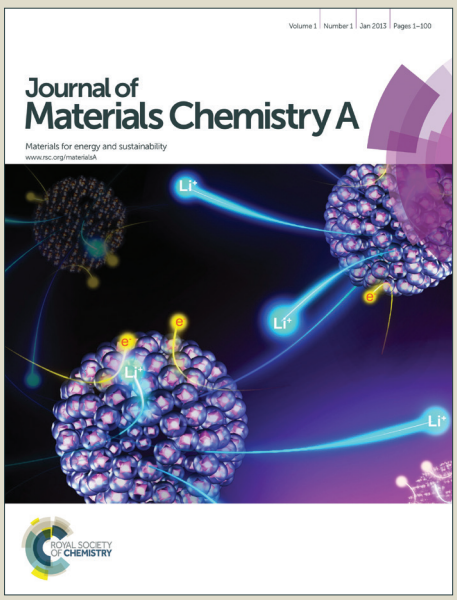

ROYAL SOCIETY OF CHEMISTRY

www.rsc.org/materialsA

Journal of Materials Chemistry A RSCPublishing

ARTICLE

A Bi-layer TiO_2 Photoanode for Highly Durable, Flexible Dye-sensitized Solar Cells

Cite this: DOI: 10.1039/x0xx00000x

Received 00th January 2012,
Accepted 00th January 2012

DOI: 10.1039/x0xx00000x

www.rsc.org/

Jianjian Lin,[a] Yong Peng,[b] Alexander R. Pascoe,[b] Fuzhi Huang,[b] Yi-Bing Cheng,*[b] Yoon-Uk Heo,[c] Andrew Nattestad,*[d] Wanchul Seung,[e] Sung Kyun Kim,[e] Hoon Joon Yoon,[e] Sang-Woo Kim,[e] Yusuke Yamauchi,[f] Shi Xue Dou,[a] and Jung Ho Kim*[a]

Low-temperature processing of dye-sensitized solar cells (DSCs) [B. Oregan, M. Grätzel, *Nature*, **1991**, 353, 737] is crucial to enable their commercialization with low-cost plastic substrates. Much of the previous work in this area has focused on mechanical compression of premade particles on plastic substrates; however, many reported that this technique did not yield sufficient interconnections for high charge carrier transport. Herein, we present bi-layer photoanodes that incorporate microstructured TiO_2 sea-urchin-like assemblies, composed of high-aspect-ratio single crystalline nanoribbons, i.e., two-dimensional subunits, which were deposited onto a nanoparticle layer (commercial P25), with a 5.6 % conversion efficiency realized. We demonstrate that this Mesoporous Hierarchical Anatase TiO_2 (MHAT) nanostructure is beneficial due to its enhanced dye loading as well as enhanced light scattering. Importantly, we also show the benefits of a bi-layer structure where the nanoribbons penetrate into the nanoparticle layer (P25) after cold isostatic pressing (CIP), resulting in improved adhesion between the MHAT top layer and the P25 under layer on the indium tin oxide-coated polyethylene naphthalate (ITO|PEN) substrate, leading to improved mechanical stability and durability, efficient electron transfer pathways, and ultimately, higher solar-to-electric conversion efficiencies.

Introduction

The tailoring of nanomaterials is paving the way toward meeting some of society's major challenges, particularly in the domain of photoelectrochemistry, with the development of water photocatalysis and dye-sensitized solar cells (DSCs), which are based on mesostructured metal oxide semiconductor and have gained attention due to their low environmental impact, their projected low capital cost (hence short energy pay-back time), and low sensitivity to temperature changes or solar incident angle, along with the fact that they can be produced in a flexible form.[1-6] The prototypical DSC is a sandwich composed of a titanium dioxide (TiO_2) photoanode, sensitized with a monolayer of organometallic dye molecules, and a platinum-coated counter electrode, with a redox electrolyte in between. High-surface-area, porous, and electronically well connected TiO_2 films serve both as a means of transport for photogenerated free charges to the external electrical contact and as a host for sensitizer molecules.

In reports of high conversion efficiency (η) DSCs, TiO_2 is generally synthesized by a hydrothermal route or sol-gel method, and made into a paste with polymeric binders, which are either screen-printed or doctor-bladed onto the conducting glass (fluorine-doped tin oxide, FTO).[7-9] This is followed by a high temperature sintering process (typically ~ 500 °C). The high temperature step is carried out to (1) remove the binders, (2) ensure better electronic connections, and (3) improve mechanical contact between particles.

Transport of injected electrons through the oxide network to the back contact is understood to occur by trap-limited diffusion, with trapping and detrapping occurring both within particles and at grain boundaries. Recombination of carriers with the oxidized species in the electrolyte at the interface can compete with this slow electron transport process, especially if the interparticle connections are weak. The limitations imposed on the electron transport by the mesoporous structure hinders progress in achieving higher η.

Flexible DSCs with plastic substrates have attracted much attention for a number of reasons including: (1) greater amenability to large-scale roll-to-roll processes than their glass-based counterparts; (2) being light weight; (3) able to be integrated into other objects (e.g. clothing).[10-17] Fabrication of flexible devices on plastic substrates, however, necessitates low-temperature processing.

Previously, low-temperature DSCs have been made by mechanically compressing the TiO_2 particles; by spraying coating binder-free colloidal TiO_2 on the conducting substrate; or by cold isostatic pressing (CIP).[18-23] One of the key objectives with these processing methods is the creation of electronic contact between particles to ensure better charge carrier transport. After deposition,

the interfaces between particles typically have poor electrical connectivity, to the detriment of electron transport through the nanoparticle film. Thus, many prior approaches to low-temperature DSC photoanode preparation have resulted in low η due to the poor particle interconnections. Early studies that focused on mechanical compression of premade particles on plastic or glass substrates did not yield sufficient interconnections for good charge carrier transport.

CIP is a powder compaction technology, which is used in materials processing engineering.[24] In this process, equal pressure is applied in all directions, resulting in better uniformity and high compaction, regardless of the electrode shape. This method was first applied as a means to prepare TiO_2 films on flexible substrates by Cheng *et al.* in 2012, however, CIP has, to date, been limited with regards to the choice of particles.[23] Either small particles (e.g., P25, 20-30 nm) or mesoporous beads (< 1 μm) comprised of ~ 10 nm features have been used.[22, 23, 25, 26] CIP has faced problems when processing larger particles, such as microspheres, which may be desirable due to their light-scattering capabilities.[9] As such, the optimization of the photoanode structure for flexible DSCs when using CIP has remained a challenge.

In this work, we demonstrate a bi-layer photoanode architecture, with good light scattering properties and improved electronic interconnections, for efficient charge percolation. Microstructured TiO_2 sea-urchin-like spherical assemblies, composed of high-aspect-ratio single-crystal nanoribbons were deposited onto a layer of nanoparticles (commercially available P25). Using this bi-layer electrode (sensitized by N719 dye and using I_3^-/I^- electrolyte), a 5.6 % conversion efficiency was obtained. This is a considerable improvement compared to P25 (4.3 %) by itself or the single spheres (5.1 %). These differences are attributed in part to enhanced dye loading and efficient light management in the hierarchical architecture. In addition, the interpenetration of the nanoribbons into the P25 under layer results in more intimate interparticle connections after a CIP step, which provides enhanced adhesion between the film and the indium-tin-oxide-coated polyethylene naphthalate (ITO|PEN) substrate, enhanced mechanical stability and durability, and efficient electron transfer pathways.

Results and discussion

Mesoporous Hierarchical Anatase TiO_2 (MHAT) particles, obtained by a facile hydrothermal process are shown in Figure 1(a) [low magnification bright-field transmission electron microscope (TEM) image] and Figure S1(a) [scanning electron microscope (SEM) image in the Supporting Information (SI)]. Uniform particle sizing spheres were achieved, which are comprised of ribbons. These can be observed in the TEM images of Figure 1(b) and (c). The specific surface area (115 $m^2 g^{-1}$) [Figure S1(b)] is higher than for either reported highly connected hierarchical textured TiO_2 spheres (103 $m^2 g^{-1}$) or P25 (42 $m^2 g^{-1}$).[9, 27] In addition, MHAT would be expected to show a higher dye-loading capacity, because of its significantly higher porosity (65.6 %) and higher roughness factor (156 μm^{-1}), compared to those of P25 (corresponding values of 34.9 % and 118 μm^{-1}, respectively).[27]

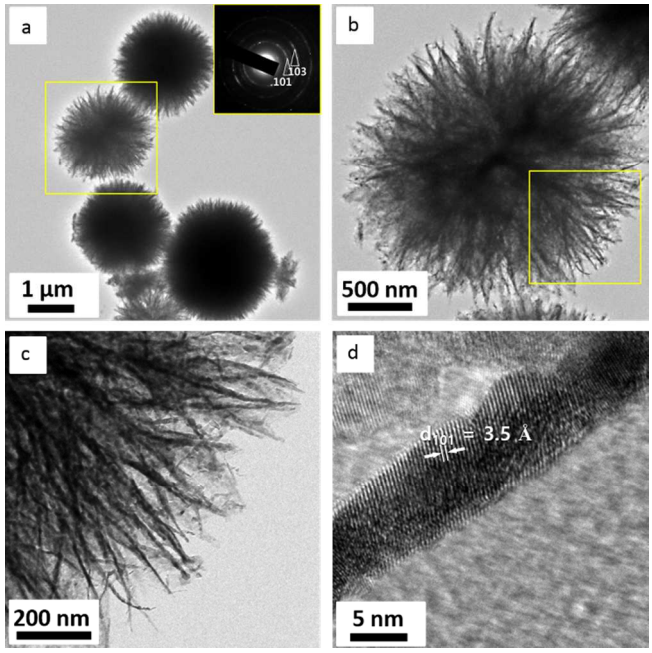

Figure 1. Characterization of mesoporous hierarchical anatase TiO_2 (MHAT): a) low magnification bright-field TEM image, with the inset showing the corresponding SAED pattern; b) TEM image of a selected sphere; c) enlarged TEM image of the marked area in (b), revealing the nanoribbon building units; d) HRTEM image of one single nanoribbon showing the fringe spacing of anatase TiO_2.

The high resolution TEM (HRTEM) image in Figure 1(d) further confirms that the MHAT is composed of single crystalline nanoribbons, with a fringe spacing of 3.5 Å, which corresponds to the (101) plane of anatase TiO_2. The selected area electron diffraction (SAED) rings [inset of Figure 1(a)] show that the TiO_2 spheres are anatase crystals, consistent with the X-ray diffraction (XRD) data [Figure S2(a)] and the Raman spectrum [Figure 2S(b)].

P25 and MHAT films [schematically shown in Figure 2(a)] with different thicknesses (6 μm and 12 μm, after CIP) were dyed with N719 and employed as electrodes in unsealed DSC devices, utilizing a I_3^-/I^- based electrolyte, with a Pt sputter-coated ITO|PEN counter electrode.

Figure 2(b) and Table S1 report the photovoltaic characteristics of the unsealed DSCs mentioned above (with *J-V* measurements completed directly after assembly). In all cases, the efficiency increased with thickness and applied pressure, predominantly as a result of an increase in the short-circuit photocurrent density (J_{sc}). For 6 μm films, the open-circuit photovoltage (V_{oc}) and fill factor (*FF*) of the MHAT-based DSCs were higher than those of the P25-based DSCs. With the highest compression force, the MHAT film (12 μm thick) showed an overall conversion efficiency of 5.1 %, an 18.0 % improvement compared to the corresponding film employing P25 (4.30 %).

Good adhesion between the TiO_2 nano-particles in the porous film, and the film with the conducting substrate is essential for achieving desirable levels of electrical conductivity and thus high efficiency of the DSC. The connection between the MHAT and the ITO|PEN substrate, however, was poor, as the large spheres have

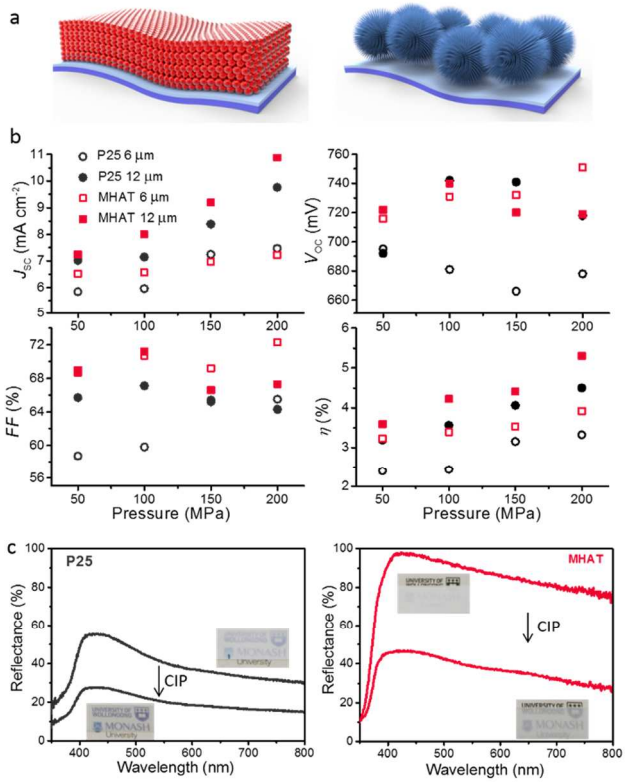

Figure 2. a) Schematic illustration of P25 and MHAT photoanode structures for flexible DSCs on ITO|PEN substrate; b) relationship between the pressure applied during a cold isostatic pressing (CIP) and the photovoltaic parameters: short-circuit photocurrent density (J_{sc}), open-circuit photovoltage (V_{oc}), fill factor (*FF*), and total power conversion efficiency (η); c) diffuse reflectance spectra of TiO_2 films before and after CIP: P25 (left) and MHAT (right), with corresponding digital photograph of P25 (12 µm) and MHAT (12 µm) films before and after CIP as insets.

limited contact with the substrate even after the CIP, further confirmed by mechanical bendability properties test (Figure 3). Films were bent at radius of 50 mm by a bending machine (further discussed in details below). From Figure 3 we can see a 40 % decrease in relative efficiency after 2000 cycles compared with 70 % for P25-based devices, demonstrating the poor connection between

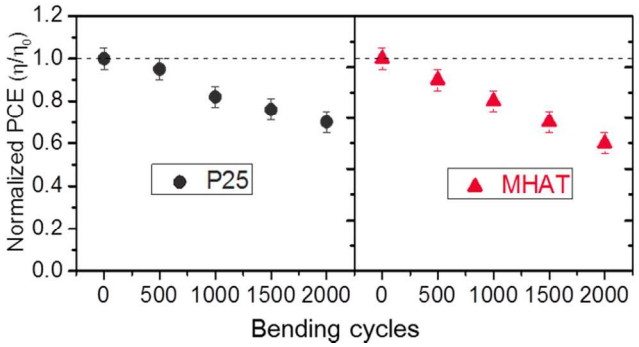

Figure 3. Normalized PCE of P25- and MHAT-based flexible DSCs as a function of bending cycles, with radius of 50 mm.

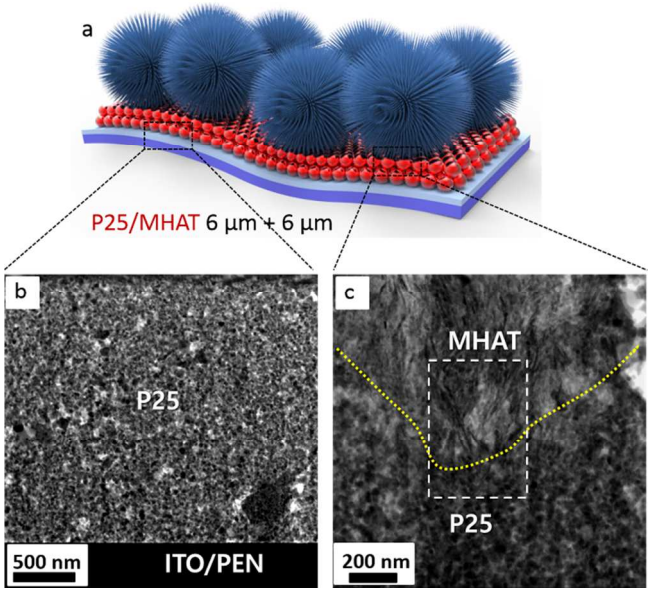

Figure 4. a) Schematic illustration of P25/MHAT (6 µm + 6 µm) photoanode structure for flexible DSCs on ITO|PEN substrate; cross-sectional BF-STEM images of P25/MHAT (6 µm + 6 µm) photoanode structure: b) shows the interface between the P25 and the ITO|PEN substrate, c) shows the interface between the P25 and the MHAT, with the highlighted part showing the MHAT nanoribbon units penetrating into the P25 nanoparticle layer.

MHAT and the ITO|PEN substrate.

To solve this problem, the MHAT material was deposited on top of a layer of P25 particles [schematically shown in Figure 4(a) and in the bright-field scanning transmission electron microscope (BF-STEM) images in Figure 4(b, c)].

During the CIP process, the two-dimensional (2D) nanoribbon building blocks of the MHAT penetrate into the P25 particle layer, improving adhesion between them [Figure 4(c)]. P25 is then able to form a good contact with the ITO|PEN substrate [Figure 4(b)]. It is well known that device performance is critically dependent on good contact between the mesoporous TiO_2 particles, as well as good adhesion between the TiO_2 particles and the substrate (ITO|PEN). In addition, as shown in the HRTEM image [Figure 1(d)], the individual nanoribbons are single-crystal in nature, which is beneficial for faster electron transportation.

Figure 5 (FE-SEM images) illustrates the surface morphology of TiO_2 films before and after pressing at 200 MPa. Uncompressed P25 film displays noticeable cracking [Figure 5(a) and Figure S3(a)]. These microcracks are formed due to shrinkage during the air-drying process in the absence of binders in the TiO_2 slurry. In addition, the films are easily scatched away from the substrate compared to the films post CIP, suggesting that the poor connection between the particles and the substrate leads to the lower J_{sc} of non-pressed P25 films. In contrast, the films post CIP had a uniform, mesoporous, and crack-free structure [Figure 5(b), Figure S3(b)].

In the MHAT and P25/MHAT films prior to CIP, the MHAT spheres are packed inefficiently with limited contact between adjacent spheres [Figure 5(c, e)]. Post application of CIP, up to 200 MPa, the MHAT spheres are much more densly packed, and it is

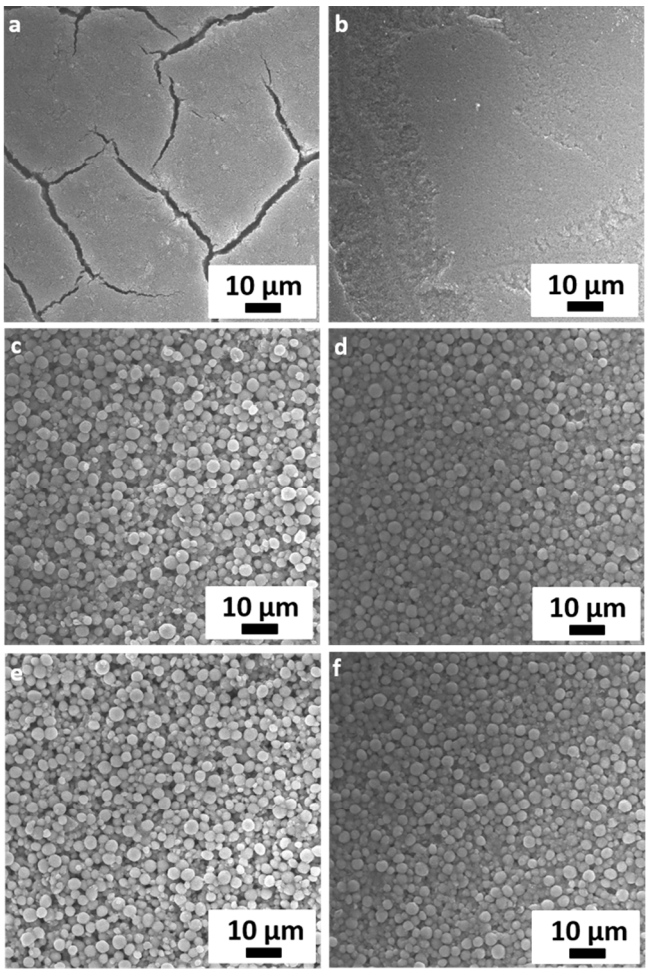

Figure 5. Low magnification FE-SEM images of different TiO_2 films on ITO|PEN substrates: P25 film a) before and b) after CIP; MHAT film c) before and d) after CIP; P25/MHAT film (e) before and (f) after CIP.

evident that this increased packing efficiency results in greater connections between the spheres [Figure 5(d, f) and Figure S3]. It is worth noting here that the MHAT spheres were not crushed by the pressing. Initially there was concern that the particles may be destroyed during CIP and that this was responsible for decreased light scattering, however, images in both Figure 4(c) and Figure 5(d, f) reveal that the spheres remain intact.

As seen by reflectance spectra [Figure 2(c)] and the photographs [the insets of Figure 2(c)], the two films pressed at 200 MPa are much more transparent than the films that had not been pressed (with the P25 film almost fully transparent).

Upon increasing the applied pressure, the connections between the particles are strengthened.[17] Unfortunately, higher pressures could not be applied due to limitations of the equipment. At 200 MPa, the diffuse reflectance spectra of the pressed MHAT films also showed a significant decrease in reflectivity compared to the films before CIP [Figure 2(c)]. The diffuse reflection capability of the pressed MHAT film, however, remains much higher than that of the pressed P25 film from 350 to 800 nm.

The photocurrent density-voltage (*J-V*) characteristic curves of P25-, MHAT- and P25/MHAT-based sealed DSCs (each with a porous TiO_2 layer ~ 12 µm in optimized thickness), are shown in Figure 6(a) (with key properties summarized in Table 1).

The P25/MHAT-based DSCs showed an average V_{oc} of 0.733 V, J_{sc} of 11.7 mA cm^{-2}, *FF* of 65.0 %, and an overall energy conversion efficiency (η) of 5.6 % under one sun conditions, much higher than the ones before CIP (4.0 %, summarized in Table S2). However, by further increasing the thickness to ~ 16 µm (12 µm P25 + 4 µm MHAT), the η was lower, with efficiency ~ 5.2 % obtained. (summarized in Table S3). Compared to P25, the higher J_{sc} for MHAT-based devices can be mainly attributed to the higher specific surface area, leading to higher dye adsorption (1.2×10^{-7} mol cm^{-2}, compared with 0.8×10^{-7} mol cm^{-2} for P25 and 1.7×10^{-7} mol cm^{-2} for P25/MHAT), based on the measured specific surface area, and porosity, as well as the light scattering properties of the MHAT films. More importantly, as observed in Figure 4(c), by depositing the MHAT onto a thin P25 layer, the MHAT nanoribbons are able to penetrate into the P25 layer, producing more intimate interparticle connections post CIP, and thus forming better contact with the ITO|PEN substrate. In addition, this enhances mechanical stability and provides efficient pathways for electron transfer. Dark current

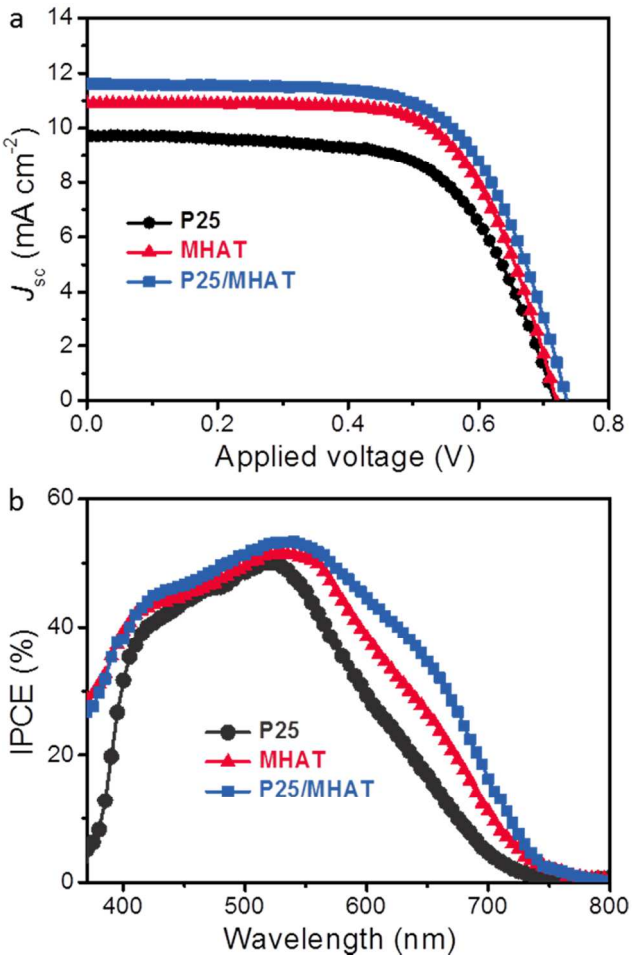

Figure 6. a) *J-V* characteristics of DSCs; b) IPCE curves of DSCs based on flexible ITO|PEN substrates covered with layers of P25 (~ 12 µm), MHAT (~ 12 µm), and a MHAT film layer over a P25 under-layer [P25/MHAT (6 µm + 6 µm)].

Table 1. Photovoltaic parameters of DSCs on flexible ITO/PEN substrates based on P25, MHAT and a MHAT film layer over a P25 under layer (P25/MHAT), which were measured under air mass (AM) 1.5 global (1.5G) one sun illumination (100 mW cm^{-2}). J_{sc}: short-circuit photocurrent density; V_{oc}: open-circuit photovoltage; *FF*: fill factor; η: total power conversion efficiency. The active areas were ~ 0.16 cm^2 for all of the cells (with the mask area 0.16 cm^2), and the data presented are the average value obtained after testing four cells and finding the standard deviation thereof.

Sample	J_{sc} [mA cm^{-2}]	V_{oc} [mV]	*FF* [%]	η [%]	Thickness[a] [μm]	Amount of dye[b] [10^{-7} mol cm^{-2}]
P25	9.4 ± 0.3	721 ± 5	64 ± 2	4.3 ± 0.2	12 ± 2	0.8
MHAT	10.9 ± 0.3	725 ± 5	64 ± 2	5.1 ± 0.2	12 ± 2	1.2
P25/MHAT	11.7 ± 0.3	733 ± 5	65 ± 2	5.6 ± 0.2	12 ± 2	1.7

[a] Measurement of film thickness was carried out on a surface profile system (Veeco Dektak 150).

[b] 0.1 M NaOH solution in mixed ethanol and water (1:1) solvent was used as the desorbent. The amount of desorbed dye was quantified by measuring its optical absorption spectrum against known concentrations.

can be used to describe the extent of the back electron transfer. From Figure S4, it can be seen that the dark current onset of the P25/MHAT-based DSC shifted to a higher potential, indicating a lower recombination rate between transferred electrons and I_3^- ions for P25/MHAT.

The incident photon to current conversion efficiency (IPCE) spectra of the devices fabricated using the three materials are shown in Figure 6(b). IPCE spectra of all the cells with N719 dye exhibited a maximum value at approximately 535 nm, where one would expect, given the dye absorbance. At this wavelength, there is minimal difference between the three films; however, in the red part of the spectrum there is substantial variation (especially in the 600-750 nm regions, where the extinction coefficient of N719 is comparatively low).

The MHAT and P25/MHAT films scattered this light more effectively than P25, giving this red light a higher probability of being absorbed. Compared to MHAT-based DSCs, P25/MHAT-based DSCs displayed a significantly higher IPCE response from 600-750 nm. In the ultraviolet-visible (UV-Vis) spectrum (Figure S5), light reflectance of the P25/MHAT film is slightly lower than that of MHAT at the same thickness. When there is a bi-layer, there is very little scattering throughout the P25, light transmitted through this layer, however, can be reflected or scattered, giving it more chance of being absorbed. Only a small amount of light will be reflected back out the front face as it will have to have made at least two passes through the P25 layer. In the case of single MHAT spheres (large particles), there is more probability that light will be reflected out of the device (through the front face) (with scheme shown in Figure S6). The result is consistent with the IPCE curves in Figure 6(b).

Figure 7 displays (a) the electron lifetime (τ_n), (b) electron diffusion coefficient ($D_{n,\,EIS}$), and (c) electron diffusion length (L_n) as measured through electrochemical impedance spectroscopy (EIS), all as functions of V_{oc}, which was controlled by adjusting the illumination intensity.[28-30] The data presented in Figure 7(d) describes the electron diffusion coefficients ($D_{n,\,IMPS}$) measured by intensity modulated photocurrent spectroscopy (IMPS). Figure 7(a) shows longer lifetimes for the two cells using the MHAT TiO_2 material, which suggests electron recombination may be slower between the MHAT TiO_2 architecture with the adjacent electrolyte species, consistent with the results studied by EIS (Figure S7). Figure 7(b) illustrates the faster charge diffusion rates achieved in a P25 film when compared to the MHAT film. This trend is equally reflected by the IMPS data in Figure 7(d). This result appears counterintuitive, given that the 2D nanoribbon unit of the MHAT should lend itself towards faster charge transfer rates than the TiO_2 nanoparticle assembly. The slower diffusion rates observed in the MHAT film, however, are expected not due to transport limitations within the 2D nanoribbons, but rather the poor electrical contact between the tips of the ribbons and the underlying substrate. When a P25 film is deposited beneath the MHAT TiO_2 network, this poor contact resistance at the tip of the ribbons is overcome, and

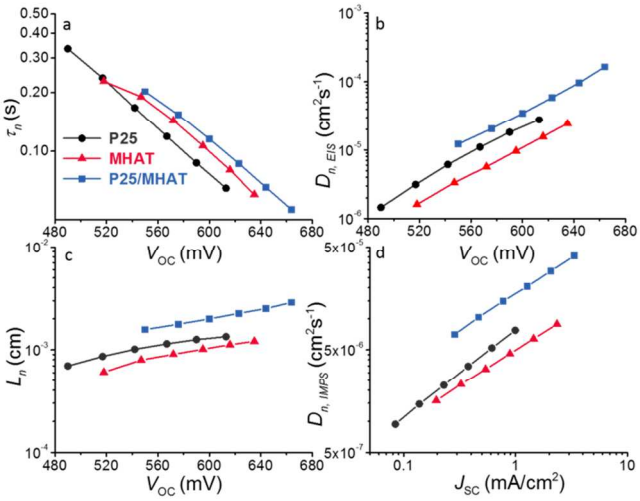

Figure 7. a) Electron lifetime (τ_n), b) electron diffusion coefficient ($D_{n,\,EIS}$), and c) electron diffusion length (L_n) as measured through impedance spectroscopy; d) electron diffusion coefficient ($D_{n,\,IMPS}$) measured though intensity modulated photocurrent spectroscopy (IMPS).

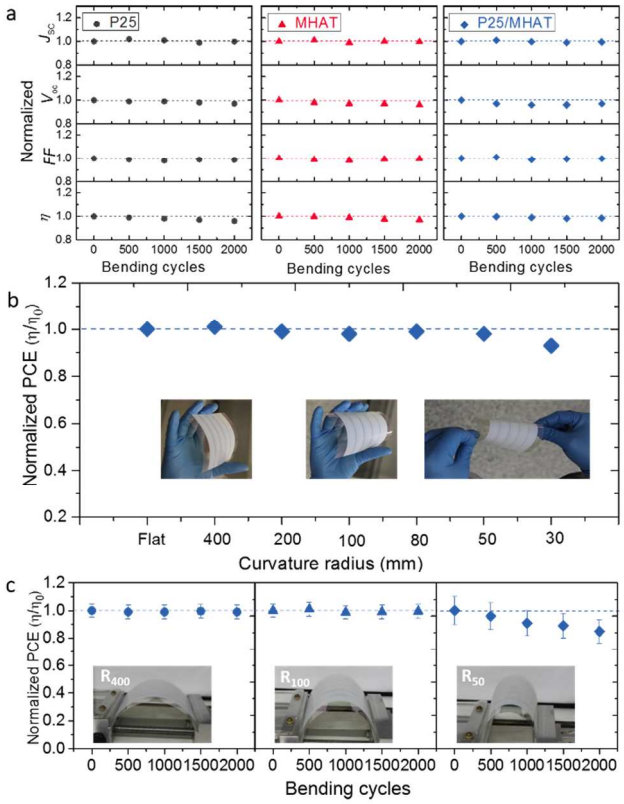

Figure 8. a) Comparison of photovoltaic properties of normalized J_{sc}, normalized V_{oc}, normalized *FF* and normalized η of P25-, MHAT-, and P25/MHAT-based flexible DSCs as a function of bending cycles, with radius of 400 mm. Bending of photoanode was performed before constructing the DSCs. Cell performances were normalized compared with the cell without bending. b) Normalized PCE of P25/MHAT-based flexible DSCs measured after bending the ITO|PEN substrate (100 cycles) within a specified radius of 400 mm to 30 mm. The insets show the digital photographs bent according to 400 mm, 100 mm, and 50 mm bending radii, respectively. c) Normalized PCE of P25/MHAT-based flexible DSCs as a function of bending radii of 400 mm, 100 mm, and 50 mm. The insets show the digital photographs bent by a bending machine during the test. The error bar represents the standard deviation from four devices.

significantly faster diffusion rates in the bi-layer film were observed, when compared to a uniform P25 film. The P25 underlayer allows the ribbons to anchor themselves to the substrate and increases the relative contact area from which electrons may be extracted. The faster diffusion rates shown in the bi-layer film indicate that transport rates within the ribbons themselves may be faster than in a conventional P25 nanoparticle film because of their single-crystal nature [Figure 1(d)]. Figure 7(c) reveals the electron diffusion lengths in the three films, measured through impedance spectroscopy. The electron diffusion lengths for all the films show a weak dependence on the illumination intensity, as predicted by the quasi-static approximation and as noted in previous work.[31, 32] This plot shows the longer electron diffusion lengths presented by the bi-layer P25 and MHAT film compared to the other two films. The slower recombination kinetics of the MHAT particles and the faster charge transport rates that they offer when coupled with the underlayer, ensure the longer diffusion lengths of the bi-layer system. This result, in combination with the increased IPCE response of the bi-layer film shown in Figure 6(b), accounts for the improved efficiencies reported for the P25 and MHAT double layered architecture.

To investigate the mechanical durability of the flexible DSCs, a bending test was performed taking into account of the bending cycles and radii. In Figure 8(a), films were bent over with radius of ~ 400 mm by a bending machine before constructing cells (with experimental procedure shown in Figure S8). No distinct decrease of the key performance indicators was observed compared to unbent films. For P25-, MHAT-, and P25/MHAT-based flexible DSCs, J_{sc}, V_{oc}, and *FF* remained identical throughout the test, which led the η constant as a function of the number of bending cycles, even after 2000 cycles of bending, demonstrating highly durability of flexible DSCs.

The η of bi-layer P25/MHAT-based flexible DSC was measured after film being bent repeatedly (100 cycles) with different radii of curvature. The PCE exhibited no significant decrease in efficiency even with 50 mm of bending radius, retaining 99 % of the original PCE value [Figure 8(b)]. The effects of mechanical bending on device performance were further evaluated during 2000 consecutive bending cycles at three different values of radii of curvature, *i.e.*, at 400 mm, 100 mm, and 50 mm, respectively (R_{400}, R_{100}, and R_{50}). The bi-layer P25/MHAT-based flexible DSCs revealed fairly promising mechanical bending stability. No significant reduction on PCE was observed when the device was bent with R_{400} or R_{100}, even after up to 2000 bending cycles. For the case of R_{50}, however, 90 % of initial PCE was retained after 1000 cycles, and further decreased to approximately 80 % after 2000 cycles (compared with 70 % and 60 % for P25-, and MHAT-based devices after 2000 cycles, with results shown in Figure S9). The above results demonstrated that the rational designed bi-layer P25/MHAT-based flexible devices possess high bending durability. As a result, the cell performance will degrade due to the limitation flexibility of ITO|PEN substrate, under an acute bending radius (< 50 mm).

Conclusions

In summary, a new photoanode architecture for cold isostatic pressing (CIP), with microstructured TiO_2 sea-urchin-like assemblies, composed of high aspect-ratio single-crystal nanoribbons deposited onto P25, was rationally designed for efficient charge transport and better light management in flexible dye-sensitized solar cells. We demonstrate that this TiO_2 nanostructure is beneficial due to enhanced dye loading as well as light scattering. We find that the interpenetration of the nanoribbons into the P25 under layer coated on the ITO|PEN film via CIP results in more intimate interparticle connections between the TiO_2 photo electrode and the ITO|PEN substrate, and enhanced mechanical stability and durability, while providing efficient electron transfer pathways. A 5.6 % solar-to-electric conversion efficiency was realized.

Experimental

Synthesis of Mesoporous Hierarchical Anatase TiO_2 (MHAT)

Acetic acid (AA, ACS reagent, ≥ 99.7 %, Sigma-Aldrich) and titanium butoxide (TB, Ti $(OCH_2CH_2CH_2CH_3)_4$, 97 %, analytical reagent, Sigma-Aldrich) were used without further purification. MHAT was prepared via a very simple acid thermal process.[9] Briefly, 1.0 mL TB, was added at room temperature to 30 mL AA solution under stirring (with stirring maintained for 24 h). This solution was then transferred to a Teflon lined reactor (Parr Instrument Company, 45 mL) and heated to 150 °C for 12 h. Afterwards, the sample was cooled before being centrifuged and sequentially washed with distilled water and ethanol (3 cycles). Following this, the samples were dried at 90 °C overnight and calcined at 500 °C for 3 h.

Materials Characterizations

XRD was employed to examine the crystal structures of the resultant products using an X-ray diffractometer (Bruker Advance, 40 kV, 30 mA) (Cu Kα, λ = 0.15406 nm) from 20º to 80º (2θ) (1 º/min), while the morphology was examined by FE-SEM (Megallan 200) and TEM (JEM-2100F). The surface area and porosity were examined using Brunauner-Emmett-Teller (BET) analysis of nitrogen adsorption-desorption data collected on a Tristar 3030 system (Micrometrics Instrument Corporation), after degassing overnight at 150 °C.

Film Fabrication and Characterizations

Titania suspensions of ~ 25 wt % were prepared by dispersing 3 g TiO_2 powders [P25 (Degussa, Hanau, Germany) and MHAT, respectively] in 99.7 % ethanol followed by ball milling.[33] Briefly, P25 (or MHAT) powders were mixed with ethanol to make a slurry with a TiO_2 content of about 30 wt% in an agate balling milling jar, with different size of agate balls. The mixture was then milled at 250 rmp speed for 2 h. Then TiO_2 films with different thicknesses were coated by the doctor-blade technique on the ITO|PEN substrates, purchased from Peccell Technologies (Kanagawa, Japan) and allowed to dry in air. These TiO_2-coated electrodes were then transferred to a polyethylene envelope (thickness ~ 80 µm) and sealed under a vacuum of 10^{-1} Torr. Vacuum-sealed electrodes were then pressed at room temperature using a cold isostatic pressing (CIP) instrument (ABB Autoclave Systems, Columbus, OH, USA) at different pressures varying between 50 and 200 MPa.[34] The surface morphology of films was examined by FE-SEM (Megallan 200) and AFM (XE-100, Park system) under ambient conditions. The Si based probe was Multi75-G produced by Budget sensors.

Fabrication of Dye-Sensitized Solar Cells

The resultant TiO_2 films were immersed in a 0.3 mM N719 (Solaronix, *cis*-bis(isothiocyanato)bis(2,2′-bipyridyl-4,4′-dicarboxylate) ruthenium(II) bis-tetra-*n*-butylammonium) dye solution in a 1:1 (v/v) mixture of acetonitrile (HPLC, Lab-scan) and *tert*-butanol (LR, Ajax Chemicals) for about 24 h. After dyeing, the samples were taken out of the dye bath, washed with acetonitrile, and dried under N_2 flow, then sandwiched with a Pt-sputtered ITO|PEN counter electrode. After that, cells were sealed together at 110 °C by using a 25 µm Surlyn (Dupont) spacer. An I^-/I_3^- organic solvent-based electrolyte solution [85:15 vol % acetonitrile/valeronitrile, 0.03 M iodine (I_2), 0.5 M 4 tertbutylpyridine (4-tBP), 0.6 M 1-butyl-3-methylimidazolium iodide (BMII), and 0.1 M guanidinium thiocyanate (GuSCN)] was introduced via vacuum back-filling. The electrolyte filling holes were blocked with an UV curable silicone glue (3M).

Solar Cell Characterizations

Dye desorption experiments were performed by washing the photoanodes in 0.1 M NaOH solution (1:1 vol ratio water : ethanol). Absorption/diffuse reflectance spectrometry of ultraviolet (UV)-visible light was used for investigating the light absorption and scattering properties (Shimadzu UV-3600). A Veeco Dektak 150 Surface Profiler was used for the film thickness measurements. *J-V* curves of the DSCs were obtained by using a Keithley 2400 Source Meter under illumination of simulated sunlight (100 mW cm^{-2}) provided by an Oriel solar simulator with an air mass (AM) 1.5 filter. Black metal with a circular aperture (4.5 in diameter) was put on top of the device during mm photovoltaic testing. IPCE spectra were recorded on a Keithley 2400 Source Meter under the irradiation of a 300 W xenon lamp with an Oriel Cornerstone™ 260 1/4 m monochromator. Electrochemical impedance spectroscopy (EIS) was performed using a 10 mV applied perturbation in the 100 mHz to 500 kHz frequency range at open-circuit under illumination. The impedance spectra were fitted using a transmission line equivalent circuit model, as reported in previous studies.[35, 36] Intensity modulated photocurrent spectroscopy (IMPS) was performed using a < 5% perturbation of the steady state illumination. EIS and IMPS data were analyzed using Zview equivalent circuit modeling software (Scribner).

Acknowledgements

This work is supported by an Australian Research Council Discovery Project (DP1096546). Dr. A. Nattestad would like to acknowledge financial support for his fellowship provided by the Australian Renewable Energy Agency (ARENA, 6-F020). J. Lin and Dr. Y. Peng contributed equally to this work.

Notes and references

[a]*Institute for Superconducting and Electronic Materials (ISEM), Australian Institute for Innovative Materials (AIIM), University of Wollongong, NSW 2522, Australia. E-mail: jhk@uow.edu.au*
[b]*Department of Materials Engineering, Monash University, Melbourne, Victoria 3800, Australia. E-mail: yibing.cheng@monash.edu*
[c]*Graduate Institute of Ferrous Technology, Pohang University of Science and Technology, San 31, Hyoja-Dong, Pohang 790-784, Republic of Korea*
[d]*Intelligent Polymer Research Institute (IPRI), ARC Centre of Excellence for Electromaterials Science, AIIM, University of Wollongong, NSW 2522, Australia. E-mail: anattest@uow.edu.au*
[e]*School of Advanced Materials Science and Engineering, Sungkyunkwan University (SKKU), Suwon 440-746, Republic of Korea.*

[f]World Premier International (WPI) Research Center for Materials Nanoarchitectonics (MANA), National Institute for Materials Science (NIMS), 1-1 Namiki, Tsukuba , Ibaraki 305-0044, Japan.

1 B. Oregan, M. Grätzel, *Nature*, 1991, **353**, 737.
2 A. Hagfeldt, G. Boschloo, L. Sun, L. Kloo, H. Pettersson, *Chem. Rev.* 2010, **110**, 6595.
3 D. Chen, R. A. Caruso, *Adv. Funct. Mater.* 2013, **23**, 1356.
4 S. K. Balasingam, M. G. Kang, Y. Jun, *Chem. Commun.* 2013, **49**, 11457.
5 F. Huang, D. Chen, X. L. Zhang, R. A. Caruso, Y.-B. Cheng, *Adv. Funct. Mater.* 2010, **20**, 1301.
6 S. Huang, Z. Yang, L. Zhang, R. He, T. Chen, Z. Cai, Y. Luo, H. Lin, H. Cao, X. Zhu, H. Sheng, *J. Mater. Chem.* 2012, **22**, 16833.
7 Y. J. Kim, M. H. Lee, H. J. Kim, G. Lim, Y. S. Choi, N.-G. Park, K. Kim, W. I. Lee, *Adv. Mater.* 2009, **21**, 3668.
8 S. Ito, P. Chen, P. Comte, M. K. Nazeeruddin, P. Liska, P. Pechy, M. Gratzel, *Prog. Photovolt: Res. Appl.* 2007, **15**, 603.
9 J. Lin, A. Nattestad, H. Yu, Y. Bai, L. Wang, S. X. Dou, J. H. Kim, *J. Mater. Chem. A* 2014, **2**, 8902.
10 J.-Y. Liao, B.-X. Lei, H.-Y. Chen, D.-B. Kuang, C.-Y. Su, *Energy Environ. Sci.* 2012, **5**, 5750.
11 Y. Peng, J. Zhong, K. Wang, B. Xue, Y.-B. Cheng, *Nano Energy* 2013, **2**, 235.
12 M. G. Kang, N.-G. Park, K. S. Ryu, S. H. Chang, K.-J. Kim, *Sol. Energy Mater*. Sol. Cells, 2006, **90**, 574.
13 W. Wang, Q. Zhao, H. Li, H. Wu, D. Zou, D. Yu, *Adv. Funct. Mater.* 2012, **22**, 2775.
14 T. Chen, L. Qiu, Z. Cai, F. Gong, Z. Yang, Z. Wang, H. Peng, *Nano Lett.* 2012, **12**, 2568.
15 W. Guo, C. Xu, X. Wang, S. Wang, C. Pan, C. Lin, Z. L. Wang, *J. Am. Chem. Soc.* 2012, **134**, 4437.
16 H. Dai, Y. Zhou, L. Chen, B. Guo, A. Li, J. Liu, T. Yu, Z. Zou, *Nanoscale* 2013, **5**, 5102.
17 F. Huang, D. Chen, Y. Chen, R. A. Caruso, Y.-B. Cheng, *J. Mater. Chem. C* 2014, **2**, 1284.
18 S. Senthilarasu, T. A. N. Peiris, J. García-Canadas, K. G. U. Wijayantha, *J. Phys. Chem. C* 2012, **116**, 19053.
19 G. Boscholl, H. Lindstrom, E. Magnusson, A. Holmberg, A. Hagfeldt, *J. Photochem. Photobiol., A* 2002, **148**, 11.
20 T. Yamaguchi, N. Tobe, D. Matsumoto, H. Arakawa, *Chem. Commun.* 2007, **45**, 4767.
21 S. Uchida, M. Tomiha, H. Takizawa and M. Kawaraya, *J. Photochem. Photobiol., A* 2004, **164**, 93.
22 H. C. Weerasinghe, F. Huang, Y.-B. Cheng, Nano Energy 2013, **2**, 174.
23 H. C. Weerasinghe, P. M. Sirimanne, G. P. Simon, Y.-B. Cheng, *Prog. Photovolt: Res. Appl.* 2012, **20**, 321.
24 R. M. Govindarajan, N. Aravas, *Int. J. Mech. Sci.* 1994, **36**, 343
25 F. Huang, D. Chen, L. Cao, R. A. Caruso, Y.-B. Cheng, *Energy Environ. Sci.* 2011, **4**, 2803.
26 H. C. Weerasinghe, P. M. Sirimanne, G. V. Franks, G. P. Simon, Y.-B. Cheng, *J. Photochem. Photobiol., A* 2010, **213**, 30.
27 J. Lin, Y.-U. Heo, A. Nattestad, Z. Sun, L. Wang, J. H. Kim, S. X. Dou, *Sci. Rep.* 2014, **4**, 5769.
28 M. Bailes, P. J. Cameron, K. Lobato, L. M. Peter, *J. Phys. Chem. B* 2005, **109**, 15429.
29 A. C. Fisher, L. M. Peter, E. A. Ponomarev, A. B. Walker, K. G. U. Wijayantha, *J. Phys. Chem. B* 2000,**104**, 949.
30 L. Peter, *Electrochem. Commun.* 1999, **1**, 576.
31 J. Bisquert, V. S. Vikhrenko, *J. Phys. Chem. B* 2004, **108**, 2313.
32 A. R. Pascoe, D. Chen, F. Huang, N. W. Duffy, R. A. Caruso, Y.-B. Cheng, *J. Phys. Chem. C* 2014, **118**, 16635.
33 H. C. Weerasinghe, P. M. Sirimanne, G. P. Simon, Y.-B. Cheng, *J. Photochem. Photobiol., A* 2009, **206**, 64.
34 Y. Peng, J. Z. Liu, K. Wang, Y.-B. Cheng, *Int. J. Photoenergy*, 2011, **2011**, 10352.
35 Q. Wang, J. E. Moser, M. Gratzel, *J. Phys. Chem. B* 2005, **109**, 14945.
36 J. Bisquert, *J. Phys. Chem. B* 2002, **106**, 325.

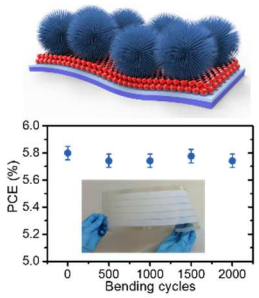

A new photoanode architecture for cold isostatic pressing (CIP), with microstructured TiO_2 sea-urchin-like assemblies, composed of high aspect-ratio single-crystal nanoribbons deposited onto P25, was rationally designed for highly durable, flexible dye-sensitized solar cells.

TOC